

Melting of icosahedral gold nanoclusters from molecular dynamics simulations

Yanting Wang and S. Teitel

*Department of Physics and Astronomy,
University of Rochester, Rochester, NY 14627*

Christoph Dellago

*Institute for Experimental Physics, University of Vienna,
Boltzmannngasse 5, 1090 Vienna, Austria*

(Dated: February 2, 2008)

Abstract

Molecular dynamics simulations show that gold clusters with about 600–3000 atoms crystallize into a Mackay icosahedron upon cooling from the liquid. A detailed surface analysis shows that the facets on the surface of the Mackay icosahedral gold clusters soften but do not premelt below the bulk melting temperature. This softening is found to be due to the increasing mobility of vertex and edge atoms with temperature, which leads to inter-layer and intra-layer diffusion, and a shrinkage of the average facet size, so that the average shape of the cluster is nearly spherical at melting.

PACS numbers:

Keywords:

I. INTRODUCTION

Nanocrystals have quite different physical properties from their corresponding bulk materials mainly because of their large surface-to-volume ratio. Among noble metals, gold nanoparticles have already shown their promise for a wide range of applications, such as nano-lithography¹, catalysts², nano-bioelectronic devices³, and ion detection⁴. Thus knowledge of the structure and stability of gold nanocrystals is of great importance.

While bulk gold has an fcc crystal structure, the competition between bulk and surface energies in nanometer sized gold crystallites can result in several different competing structures^{5,6}. One such structure which has been observed both in simulations^{7,8} and in experiments^{9,10} is the “Mackay icosahedron”^{11,12}, which we will also denote as the “Ih structure”, consisting of 20 slightly distorted fcc tetrahedra, with four $\{111\}$ facets each, meeting at the center to form an icosahedral shaped cluster. The internal facets of the tetrahedra meet at strain inducing twin grain boundaries with a local hcp structure, leaving the cluster with 20 external $\{111\}$ facets. For an Ih structure with L shells, the magic number of atoms needed to construct a perfectly symmetric ideal icosahedron is¹²,

$$N_L = \frac{10}{3}L^3 + 5L^2 + \frac{11}{3}L + 1. \quad (1)$$

In Fig. 1 we show the atomic configuration for an ideal Ih structure with the magic number of $N = 2869$ atoms ($L = 9$). Atoms are shaded to indicate local fcc, hcp, or other structure.

Different theoretical and numerical models have indicated different limits for the stability of such Ih clusters. Using a continuum approach to take into account the strain energy and the twin grain boundary energy, Ino predicted that icosahedral clusters should be stable up to sizes of 40 000 atoms¹³. Similar stability limits for icosahedral gold clusters were predicted by Marks using a modified Wulff construction^{9,14}. More recent atomistic calculations^{15,16,17} find that, at $T = 0$, icosahedral gold nanoclusters are the lowest energy structure only in a very small size range of tens of atoms; other structures, such as an fcc crystal with a truncated octahedral shape, become energetically favored at larger sizes. However, in molecular dynamics simulations of the freezing of gold nanoparticles Chushak and Bartell⁷ observed icosahedral particles of up to almost 4000 atoms. Simulations by Cleveland *et al.*⁶ found that when fcc truncated-octahedral gold clusters with hundreds of atoms were heated, they underwent a transformation to the icosahedral structure.

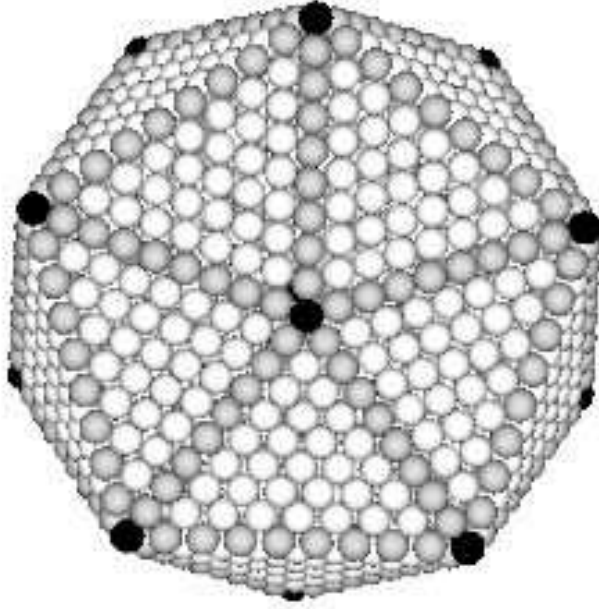


FIG. 1: An ideal Ih structure with the magic number of 2869 atoms. Atoms are shaded to indicate their local structure: fcc is white, hcp is gray, and other is black.

While the theoretical limit of stability of Ih structures thus remains unclear, and their formation may involve kinetic rather than strictly equilibrium effects^{9,13,14,15,16,17}, it is natural to suppose that the formation of the Ih structure is related to the very high stability of the $\{111\}$ external surfaces. Simulations¹⁸ and experiments¹⁹ on bulk slab-like geometries with exposed $\{111\}$ surfaces have shown that, unlike the $\{100\}$ and $\{110\}$ surfaces which melt below the bulk melting temperature T_m , the $\{111\}$ surface is a nonmelting surface without roughening, wetting, or melting up to the bulk melting temperature T_m , and can in fact lead to superheating of the solid²⁰. In light of this observation it is interesting to consider how the high stability of the $\{111\}$ facets effects the melting and equilibrium shape of such icosahedral clusters.

In this paper, we will show, by molecular dynamics (MD) simulations, that liquid gold clusters with about 600–3000 atoms crystallize into an Ih structure, with a missing central atom, upon cooling from the liquid. We then reheat the clusters back through the melting transition at temperature T_m . Unlike many previous simulations which simulate a continuous heating process, we simulate heating in quasi equilibrium, running for a long simulated time (43 ns) at each temperature, before increasing the temperature. We pay careful attention

to the behavior of the cluster surface, and compute for the first time the *average* cluster shape, as we pass through T_m . Using careful measurements of both bond orientational order parameters and atomic diffusion we find that the $\{111\}$ facets of the cluster surface stay ordered and do not premelt or roughen below the cluster melting temperature T_m . Nevertheless, we find that there is a considerable softening of the cluster surface roughly ~ 200 K below T_m that can be regarded as due to the “melting” of the atoms on the vertices and edges of the cluster. As temperature increases, there is an increasing mobility of these atoms leading to intra-layer and inter-layer diffusion, and a shrinkage of the average area of the $\{111\}$ facets. The equilibrium shape progresses from fully faceted, to faceted with rounded edges, to nearly spherical just below T_m . Throughout this region, the interior atoms of the cluster remain essentially perfectly ordered, until T_m is reached. Our results refine those of earlier simulations of gold clusters^{6,21,22}, which used measurements of the radial density distribution and the observation of surface diffusion as evidence for a general premelting of the cluster surface. A preliminary report of some of our results has been presented in Ref. 23.

II. METHODS

A. Simulation model and methods

On modern computers *ab initio* simulation techniques providing an accurate description of interaction energies can be used to simulate systems consisting of up to hundreds of atoms²⁴. However, such methods are too computationally demanding to allow long simulation times. Using less accurate but computationally less expensive model potentials, such as the embedded atom method²⁵, the Murrell-Mottram potential²⁶, the Lennard-Jones potential²⁷, the Morse potential²⁸, the many-body Gupta potential²⁹, or the many-body “glue” potential³⁰, one can extend the size of simulated gold nanoclusters to more than ten thousand atoms. In this study, we have chosen the many-body “glue” potential because it was found to yield an accurate description of the bulk, defect and surface properties of gold³⁰. In the “glue” model, the potential energy of a system of N atoms consists of a sum of pair potentials ϕ and a many-body “glue” energy U ,

$$V = \frac{1}{2} \sum_i \sum_{j \neq i} \phi(r_{ij}) + \sum_i U(n_i). \quad (2)$$

Here the sums run over all particles, $r_{ij} = |\mathbf{r}_i - \mathbf{r}_j|$ is the interatomic distance between atoms i and j , and $\phi(r)$ is the pair interaction energy. The many-body “glue” energy $U(n_i)$ depends on an effective coordination number n_i of atom i , which is defined by

$$n_i = \sum_j \rho(r_{ij}). \quad (3)$$

Here $\rho(r)$ is a short-ranged monotonically decreasing function of the interatomic distance r . We use the specific forms for the pair potential $\phi(r)$, and the glue terms $U(n)$ and $\rho(r)$, as given by Ercolessi *et al.* in Ref. 30.

We will simulate our gold clusters by treating each atom as a classical particle. Newton’s equations of motion are integrated using the velocity Verlet algorithm³¹ with a time step of $\Delta t = 35$ fs. Because the many-body “glue” potential uses a cutoff, a cell index method can be used to reduce the computational time³². In this method, the simulation box is divided into cubic cells with side lengths larger than the cutoff distance (3.9 Å for the gold glue model). When calculating energies and forces one considers only interactions between atoms within the same cell and the neighboring 26 cells. This approach reduces the required computation time from order N^2 to order N . On a PC equipped with a 1.5 GHz AMD Athlon CPU and 1 GB of memory, 25 000 steps can be carried out per CPU-hour for a system of 2624 atoms propagating the system for about 100 ps.

We will refer to each time step Δt of the velocity Verlet algorithm as one basic molecular dynamics (MD) step. Since each MD step is an integration of Newton’s equation, it necessarily conserves the total energy of the system, and thus simulates a microcanonical ensemble. To sample instead in the canonical ensemble, we supplement this basic MD step according to two different well known methods. The Andersen thermostat³³ is a method that mimics a system coupled to a heat bath with constant temperature. At the end of each MD step, each particle of the cluster is, with probability $p \sim 0.03\%$, assigned a new velocity sampled randomly from the Boltzmann distribution of a given temperature. The Andersen thermostat samples both configuration and momentum spaces according to the canonical distribution, so that the instantaneous total kinetic energy fluctuates, as is the case for a real physical system. However, the Andersen thermostat method does not conserve the total linear and angular momenta, and so will cause the system’s overall position and orientation to drift over the course of the simulation. This would complicate our analysis of cluster shape as well as atomic diffusion, since we want to measure these quantities with respect to

coordinates that stay fixed with respect to the cluster.

This drawback of the Andersen thermostat can be avoided using the Gaussian isokinetic thermostat³⁴ which keeps the total kinetic energy K of the system fixed at a value corresponding to a given temperature T , $K = (3/2)Nk_B T$. We implement this thermostat by rescaling all velocities by a constant factor after each basic MD step so as to conserve the total kinetic energy. Although the Gaussian isokinetic dynamics does not sample the canonical distribution in momentum space, this method does correctly sample configuration space and so yields correct equilibrium averages of all structural quantities that depend on positional coordinates only. This “constant temperature” method has the advantage of conserving both total linear and angular momenta, thus keeping the cluster at a fixed position and orientation.

In our simulations, our first goal will be to cool our cluster to low temperature from a liquid melt to see what solid structure forms. To do this we use the Andersen thermostat method since we believe it models more closely the true dynamics of the physical system, and hence will incorporate effects that may be due to kinetics rather than just pure thermodynamics. Later, to observe the equilibrium shape and other properties of the cluster, we will use the constant temperature MD to heat back through melting. This will keep the cluster position and orientation fixed, and so simplify our analysis.

B. Quantifying structure by bond orientational order parameters

To determine the crystalline structure of our gold nanoclusters, we will use the method of bond orientational order parameters³⁵, which we now review. The idea of the bond order parameters is to capture the symmetry of bond orientations regardless of the bond lengths. A bond is defined as the vector joining a pair of neighboring atoms. Throughout our paper, we will define the neighboring atoms of a given atom i as those atoms which have an interatomic distance less than a cutoff radius of 3.8 Å, equal to the distance to the minimum between the first and the second peaks of the pair correlation function. The local order parameters associated with a bond \mathbf{r} are the set of numbers,

$$Q_{lm}(\mathbf{r}) \equiv Y_{lm}(\theta(\mathbf{r}), \phi(\mathbf{r})), \quad (4)$$

where $\theta(\mathbf{r})$ and $\phi(\mathbf{r})$ are the polar and azimuthal angles of the bond with respect to an arbitrary but fixed reference frame, and $Y_{lm}(\theta(\mathbf{r}), \phi(\mathbf{r}))$ are the usual spherical harmonics. Since the bond between atoms i and j may be arbitrarily taken as either \mathbf{r}_{ij} or $\mathbf{r}_{ji} = -\mathbf{r}_{ij}$, it is useful to consider only the even- l bond parameters Q_{lm} , since only these are invariant to such bond inversions. Global bond order parameters can then be calculated by averaging $Q_{lm}(\mathbf{r})$ over all bonds in the cluster,

$$\overline{Q}_{lm} \equiv \frac{1}{N_b} \sum_{\text{bonds}} Q_{lm}(\mathbf{r}), \quad (5)$$

where N_b is the number of bonds. To make the order parameters invariant with respect to rotations of the reference frame, the second-order invariants are defined as,

$$Q_l \equiv \sqrt{\frac{4\pi}{2l+1} \sum_{m=-l}^l |\overline{Q}_{lm}|^2}, \quad (6)$$

and the third-order invariants are defined as,

$$W_l \equiv \sum_{m_1, m_2, m_3} \begin{pmatrix} l & l & l \\ m_1 & m_2 & m_3 \end{pmatrix} \overline{Q}_{lm_1} \overline{Q}_{lm_2} \overline{Q}_{lm_3}, \quad (7)$$

$$m_1 + m_2 + m_3 = 0$$

where the coefficients (\cdots) are the Wigner $3j$ symbols³⁶. It is standard to define a normalized quantity,

$$\hat{W}_l \equiv \frac{W_l}{\left(\sum_m |Q_{lm}|^2\right)^{3/2}} \quad (8)$$

which, for a given l , is independent of the magnitudes of the $\{Q_{lm}\}$.

The four bond order parameters Q_4 , Q_6 , \hat{W}_4 , \hat{W}_6 are generally sufficient to identify different crystal structures. In Table I we give their values for ideal periodic fcc, hcp, sc, and bcc crystal structures. Since the Ih structure is not periodic, it may in principle have values for the bond order parameters that depend on the cluster size. In Fig. 2(a) we plot the values of the four bond orientational order parameters vs. the cluster size N for several ideal Ih structures. Although there is a strong size dependence for small clusters, the bond parameters saturate to well defined values as N increases, and we list these in Table I. Note that although, for large N , most of the atoms in the Ih structure have a local fcc structure, the values of the bond order parameters are different from those of a pure fcc crystal; this is

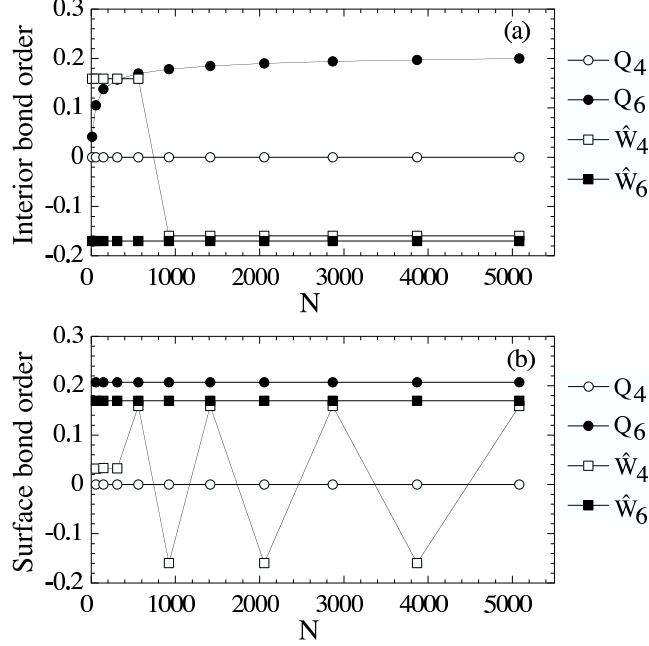


FIG. 2: The values of (a) the bulk and (b) the surface bond orientational order parameters vs. the cluster size N , for ideal icosahedral clusters with magic numbers N .

TABLE I: Bond order parameters for face-centered-cubic (fcc), hexagonal close-packed (hcp), simple cubic (sc), body-centered-cubic (bcc), liquid, Ih bulk, and Ih surface structures.

Geometry	Q_4	Q_6	\hat{W}_4	\hat{W}_6
fcc	0.190 94	0.574 52	-0.159 32	-0.013 16
hcp	0.097 22	0.484 76	0.134 10	-0.012 44
sc	0.763 76	0.353 55	0.159 32	0.013 16
bcc	0.082 02	0.500 83	0.159 32	0.013 16
liquid	0	0	0	0
Ih bulk	0	0.199 61	-0.159 32	-0.169 75
Ih surface	0	0.207 29	$\pm 0.159 32$	0.169 75

due to averaging the order parameters over the differing orientations of the 20 fcc tetrahedra that make up the Ih structure.

The bond orientational order parameters, averaged over all bonds, will be used to monitor global structural changes of our cluster. In particular, a large liquid cluster will have vanishing values for the bond order parameters. Thus the decay of the bond parameters from

their finite low temperature values to zero will be a signature of the melting transition. In this work we will be particularly concerned with the behavior of atoms on the surface of the cluster. Surface structures of nanomaterials can often be quite different from the bulk. We therefore will consider separately the *bulk* bond order parameters, computed by averaging over only those bonds connecting atoms that are in the internal “bulk” of the cluster, vs. the *surface* bond order parameters, computed by averaging over only those bonds connecting pairs of atoms that lie on the surface of the cluster. In Fig. 2(b) we plot the values of such surface bond order parameters for an ideal Ih structure vs. cluster size N . Again we see that they approach well defined constants as N increases, except for \hat{W}_4 which oscillates. The values of these large N surface bond parameters are listed in Table I. Note that for the same Ih structure, the bulk bond parameters have different values than the surface bond parameters, since they are measuring properties of three dimensional vs. two dimensional structures, respectively.

C. Geometrical analysis of the surface

A main goal of this work is to quantify the geometrical behavior of the surface of the gold nanocluster. In this section we describe the algorithms that we use for this characterization.

1. Cone algorithm

The first step in our analysis is to identify the surface particles of the clusters accurately according to their geometrical positions. We have developed a new algorithm, which we call the “cone” algorithm, to do this. For a given particle, we define an associated *cone region* as the region inside a cone of side length a and angle θ , whose vertex resides on the particle. A *hollow cone* is a cone region with no other particles inside it. We take a particle to be on the surface if at least one associated hollow cone can be found.

The cone algorithm is intrinsically consistent with the general definition of surface particles. It can pick up all of the particles on a convex surface. For the particles on a concave surface, the precision of identifying a surface atom relies on the choice of the parameters a and θ (see Fig. 3). By visual examination of our generated configurations, we found that the two parameters $a = 5.0 \text{ \AA}$ and $\theta = \pi/3$ gave good results for our clusters. For a gold

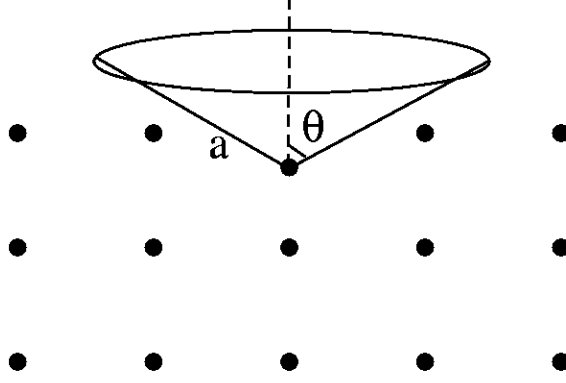


FIG. 3: Schematic of the cone algorithm.

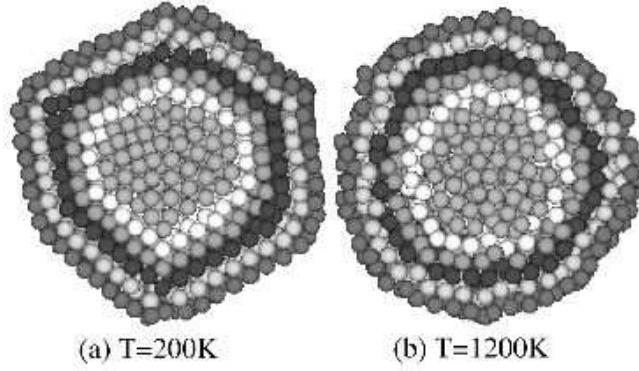


FIG. 4: Cross section of a gold cluster with 2624 atoms at (a) $T = 200$ K in an Ih structure and (b) $T = 1200$ K in the liquid, with the 5 topmost layers, as determined by the cone algorithm, marked by different gray scales.

cluster with 5082 atoms, a complete determination of the surface atoms requires less than 2 s of CPU time. The cone algorithm can also be applied recursively to divide particles into surface and sub-surface layers to allow inter-layer analysis. Fig. 4 shows a planar slice cut through an instantaneous configuration of a gold cluster with 2624 atoms at (a) $T = 200$ K in an Ih structure and (b) $T = 1200$ K in the liquid, respectively. From this figure we can see that the cone algorithm works well on both solid and liquid configurations.

2. Curvature

Having identified the surface particles, we next want to quantify the surface morphology of the clusters. To do this, we compute two different measures of the surface curvature, the *bond curvature* and the *maximal local surface curvature*, as defined below.

Our first step is to determine a tangent plane to the cluster surface at each surface particle. To do this, we consider the collection of particles determined by the particle of interest and all its neighboring particles which are also on the surface. Denote the coordinates of these particles by $\mathbf{r}_i \equiv (x_i, y_i, z_i)$, $i = 1 \dots N_s$, where N_s is the number of the particles under consideration. We define the tangent plane to pass through the center of mass of these particles, and we determine its orientation by minimizing the mean square distance of the particles to the plane. Specifically, we solve for this plane as follows. If $\hat{\mathbf{n}} \equiv (n_x, n_y, n_z)$ is the unit normal vector of the tangent plane and $\mathbf{r}_c \equiv (x_c, y_c, z_c)$ is the coordinate of the center of mass, then the distance from the i th particle to the tangent plane is,

$$d_i = \hat{\mathbf{n}} \cdot (\mathbf{r}_i - \mathbf{r}_c). \quad (9)$$

We determine the normal vector $\hat{\mathbf{n}}$ by minimizing $\sum_i d_i^2$ subject to the constraint $\hat{\mathbf{n}}^2 = 1$. Introducing an undetermined Lagrange multiplier λ , we solve for,

$$\frac{\delta}{\delta \mathbf{n}} \left[\sum_i d_i^2 - \lambda (\hat{\mathbf{n}}^2 - 1) \right] = 0. \quad (10)$$

Eq. (10) leads to the symmetric eigenvalue problem,

$$\begin{pmatrix} XX - \lambda & XY & XZ \\ XY & YY - \lambda & YZ \\ XZ & YZ & ZZ - \lambda \end{pmatrix} \begin{pmatrix} n_x \\ n_y \\ n_z \end{pmatrix} = 0, \quad (11)$$

where $XY = \sum_i (x_i - x_c)(y_i - y_c)$, and other quantities are computed similarly. The smallest of the three possible eigenvalues λ determines the minimum value of $\sum_i d_i^2$, and its associated eigenvector (n_x, n_y, n_z) is the normal vector $\hat{\mathbf{n}}$ of the tangent plane.

We now define the *bond curvature*, c_b , of a bond connecting two neighboring surface particles. Consider two neighboring surface particles at positions \mathbf{r}_1 and \mathbf{r}_2 and let $\hat{\mathbf{n}}_1$ and $\hat{\mathbf{n}}_2$ be the unit normal vectors of their corresponding tangent planes. We can uniquely fit a circle that passes through the two points, such that $\hat{\mathbf{n}}_1$ and $\hat{\mathbf{n}}_2$ are normal to the circle. The

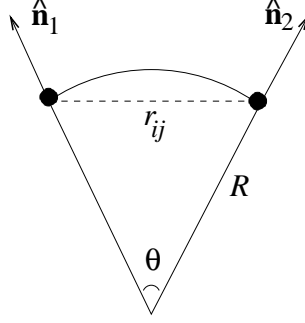


FIG. 5: Schematic for the calculation of the bond curvature.

bond curvature c_b is then defined in terms of the radius R of this fitted circle,

$$c_b \equiv \frac{1}{R} = \frac{2\sin(\theta/2)}{r_{ij}}, \quad (12)$$

where $\theta = \text{acos}(\hat{\mathbf{n}}_1 \cdot \hat{\mathbf{n}}_2)$ is the angle between the two normal vectors and $r_{ij} = |\mathbf{r}_1 - \mathbf{r}_2|$ is the distance between the two particles. The geometry of this fit is illustrated in Fig. 5.

Alternatively, we can compute the *surface curvature* at each particle on the surface as follows. Consider a particle on the surface, and all its neighboring particles that are also on the surface. Since the geometry of these points roughly defines a surface in 3D space, we find the best fit of a paraboloid surface to these points. The *maximal local curvature*, κ_M , and the *minimal local curvature*, κ_m , are then given by the two principal curvatures of the fitted paraboloid. The schematic of this method is shown in Fig. 6. To fit the paraboloid at the surface particle \mathbf{r}_0 , we take the normal vector $\hat{\mathbf{n}}$ to the tangent surface at \mathbf{r}_0 , as computed above, and define this to be the local z -axis. We place the origin at \mathbf{r}_0 and then choose arbitrary but fixed x and y axes in the tangent plane. We then define the coordinates (x_i, y_i, z_i) of neighboring particle \mathbf{r}_i in this coordinate system. We then choose a paraboloid function,

$$f(x, y) = a_{xx}x^2 + 2a_{xy}xy + a_{yy}y^2, \quad (13)$$

and fit it through the neighboring points \mathbf{r}_i by minimizing

$$S = \sum_i (z_i - f(x_i, y_i))^2, \quad (14)$$

with respect to a_{xx} , a_{xy} , and a_{yy} . This leads to the following set of linear equations,

$$\begin{pmatrix} \sum_i x_i^4 & \sum_i x_i^3 y_i & \sum_i x_i^2 y_i^2 \\ \sum_i x_i^3 y_i & \sum_i x_i^2 y_i^2 & \sum_i x_i y_i^3 \\ \sum_i x_i^2 y_i^2 & \sum_i x_i y_i^3 & \sum_i y_i^4 \end{pmatrix} \begin{pmatrix} a_{xx} \\ 2a_{xy} \\ a_{yy} \end{pmatrix} = \begin{pmatrix} \sum_i x_i^2 z_i \\ \sum_i x_i y_i z_i \\ \sum_i y_i^2 z_i \end{pmatrix}. \quad (15)$$

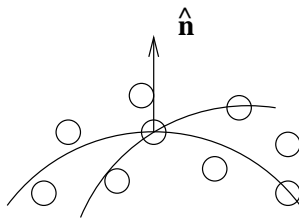


FIG. 6: Schematic for the calculation of the local surface curvatures.

Solving Eq. (15) for a_{xx} , a_{xy} , a_{yy} , we diagonalize the symmetric matrix with the elements $a_{\mu\nu}$ to obtain the two principal axes and the corresponding eigenvalues λ_1 and λ_2 . The local curvatures are then given by $\kappa_{1,2} = \frac{1}{2}\lambda_{1,2}$. We will see that the maximal local curvature will be very helpful for visualizing the vertex, edge and facet atoms of the cluster surface.

To test these two methods, we consider the ideal Ih gold cluster with a magic number of atoms $N = 2869$, shown in Fig. 1. In Fig. 7 (top row) we show the resulting histograms of bond curvature and maximal local curvature for this cluster. Both histograms consist solely of δ functions, corresponding to the facets, the edges and the vertices of the Ih structure. For the bond curvature histogram there are *two* separate peaks for the vertices, corresponding to the bond curvatures between the vertex atoms and the edge atoms, and the vertex atoms and the facet atoms. We also test our method for the average shape of a liquid gold cluster with 2624 atoms at $T = 1200$ K (shown in Fig. 8(c)). We show our results in Fig. 7 (bottom row). Both histograms have just one peak of finite width, centered at $1/R = 0.047 \text{ \AA}^{-1}$, with $R = 21.5 \text{ \AA}$ the radius of the spherical liquid drop. Note that while the average shape of the liquid drop is close to a perfect sphere, the histogram of its curvatures seems relatively broad. We have found that this is due to the small discrete number of neighboring surface particles that is used to define the fitted paraboloid. Even small deviations of these particles from a constant radius can lead to noticeable variations in the fitted curvatures. We find that we can reduce the width of the curvature histogram for the liquid cluster by increasing the cutoff length used to define neighboring particles, and so have more particles included in the fits to the local paraboloids. However, while this improves the calculation for a spherical cluster, it makes it worse for high curvature regions near edges and vertices in an Ih cluster, where curvature varies rapidly as one moves across the surface. With this understanding of our method's limitations, we therefore leave our cutoff as given above.

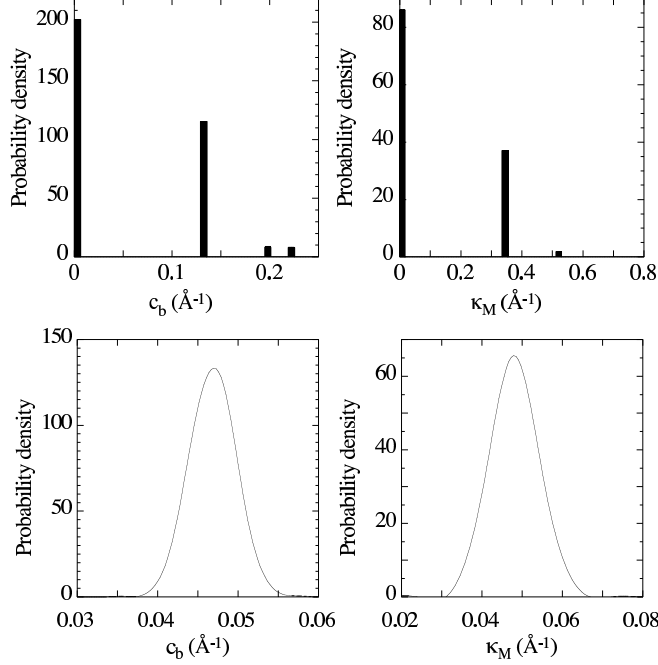


FIG. 7: Histograms of bond curvature c_b and maximal local curvature κ_M of (i) top row: an ideal Ih cluster with $N = 2869$ atoms, and (ii) bottom row: the average shape of a liquid cluster with $N = 2624$ atoms.

3. Average shape

At low temperatures, the atoms in the gold cluster remain at well defined equilibrium positions and only thermally oscillate around the vicinity of these equilibrium positions. The shape of the cluster is thus easily determined from an instantaneous configuration. At high temperatures, however, atoms become more mobile and the macroscopic shape of the cluster fluctuates dramatically from configuration to configuration. In this case it becomes necessary to average over many fluctuating configurations to define the average cluster shape. Since our constant temperature MD conserves total linear and angular momenta and both are set to zero, the configurational shape changes we average over represent fluctuations of the surface atoms rather than trivial shifts or rotations of the cluster as a whole.

At high temperatures, simply averaging the position of each atom throughout the course of the simulation does not give the average shape because the atoms are in general no longer bound to specific sites but may diffuse many interatomic spacings through the cluster. We therefore use the following approach to define the average cluster shape. We divide the surface of the cluster into equal solid angles, and then average the instantaneous surface

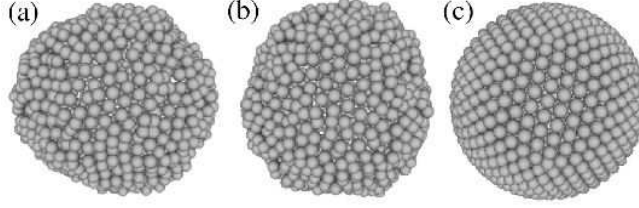


FIG. 8: A liquid gold cluster with 2624 atoms at $T = 1200$ K. (a) and (b) are two instantaneous configurations. (c) is the shape averaged over 1000 such instantaneous configurations.

atom positions in each solid angle. This average position in each solid angle then defines the profile of the cluster's average shape. This average shape does not contain information about the individual surface atom positions, since generally a given solid angle may contain the instantaneous positions of different surface atoms at different times. To define our solid angle division, we use the best covering spherical codes with icosahedral symmetry³⁷ to divide the 4π total solid angle of the sphere centered at the center of mass into cone cells with almost equal solid angles. Choosing different numbers of solid angles results in different resolutions; we always choose a number of solid angles that matches as close as possible to the number of surface atoms in the cluster.

We illustrate this method for a liquid gold cluster with 2624 atoms at $T = 1200$ K. In Figs. 8(a) and (b) we show two arbitrary instantaneous configurations of the cluster. Theoretically, a liquid cluster should have a perfect sphere as the equilibrium shape. However, we see that the instantaneous configurations can have noticeably large fluctuations about the average shape. Applying our shape averaging procedure above on 1000 configurations sampled at equal time intervals from 43 ns of simulated time, we recover that the average shape, shown in Fig. 8(c), is a perfect sphere as expected. Note that in Figs. 8(a) and (b), the small spheres represent instantaneous atomic positions. In contrast, in Fig. 8(c), they represent not specific atoms, but rather the average surface position within the given solid angle.

D. Atom diffusion analysis

With enough kinetic energy, atoms can hop around their crystal sites and even travel across the whole cluster. The mean squared displacement (MSD)³¹, $\Delta r^2(t)$, is a convenient

way to measure the average movement of a group of atoms. It is defined as

$$\Delta r^2(t) = \frac{1}{MN_s} \sum_{j=1}^M \sum_{i=1}^{N_s} [\mathbf{r}_i(t_j + t) - \mathbf{r}_i(t_j)]^2, \quad (16)$$

where \mathbf{r}_i , $i = 1 \dots N_s$ are the positions of the N_s atoms under consideration, and t is the time interval over which the motion takes place. We average over M non-overlapping time intervals, with $t_j \equiv t_{j-1} + t$. For an infinite three dimensional bulk system, we expect that $\Delta r^2 = 6Dt$ as $t \rightarrow \infty$, where D is the diffusion coefficient. In a finite cluster, however, the MSD will eventually saturate on a length scale comparable to the cluster size. We therefore determine the diffusion coefficient D by fitting $\Delta r^2(t)$ to the early time linear part before saturation takes place.

We will also find that a convenient way to visualize individual atomic displacements is through an *ellipsoid of displacement*. We compute this ellipsoid as follows. For a given atom traced through K successive configurations for a simulation time t , the mean squared displacement correlations are given by the 3×3 matrix \mathbf{C} with elements,

$$C_{\mu\nu} \equiv \frac{1}{K} \sum_{i=1}^K (r_{i\mu} - \langle r_\mu \rangle)(r_{i\nu} - \langle r_\nu \rangle), \quad (17)$$

where $\mu, \nu = x, y, z$, $r_{i\mu}$ is the μ -coordinate of the atom in configuration i , and $\langle r_\mu \rangle$ is the average of the coordinate over all K configurations. The probability for the atom to be at position \mathbf{r} is then approximated as $P(\mathbf{r}) \sim \exp(-\frac{1}{2}[(\mathbf{r} - \langle \mathbf{r} \rangle) \cdot \mathbf{C}^{-1} \cdot (\mathbf{r} - \langle \mathbf{r} \rangle)])$, and so the surface of our ellipsoid of displacement is given by the equation,

$$(\mathbf{r} - \langle \mathbf{r} \rangle) \cdot \mathbf{C}^{-1} \cdot (\mathbf{r} - \langle \mathbf{r} \rangle) = 1. \quad (18)$$

The eigenvectors of $C_{\mu\nu}$ and the square root of their corresponding eigenvalues then define the axes and principal radii of the ellipsoid, which we center on the average atom position $\langle \mathbf{r} \rangle$. This ellipsoid provides a convenient visualization of the directional distribution of root mean squared displacements over the time t .

III. RESULTS

In this section we report on our results. Gold clusters with more than 5000 atoms require too much computational time to allow for the long simulation times we want in order to explore the equilibrium behavior. Clusters with fewer than a few hundred atoms,

however, have large finite size effects due to the larger surface-to-volume ratio. Such smaller clusters can undergo transitions between several different crystal structures even at low temperatures^{6,22,38}, and they have less sharply defined melting transitions. In this work we have therefore simulated several clusters in the range of 600 to 5000 atoms. In our results below, we will concentrate on the moderate size of $N = 2624$ atoms, for which we have done our most complete and careful analysis. We will also give less detailed results for two smaller sizes, $N = 603$ and $N = 1409$, in order to illustrate general trends. Note that these values of N are *not* among the magic numbers (see Eq. (1)) needed to construct a perfect Mackay icosahedron. Nevertheless we will show that these clusters still form Ih structures upon cooling. We have also studied several clusters *with* a magic number of atoms, by explicitly constructing the Mackay icosahedron at low temperature, and heating through melting. We will give results for sizes³⁹ $N = 922$ and $N = 5082$ in order to compare with the other more generic values of N .

A. Mackay icosahedra with a missing central atom

Our initial goal is to cool a liquid cluster through the melting transition to determine the ordered structure into which it solidifies. We therefore started with a liquid gold cluster with $N = 2624$ atoms which we roughly equilibrated at 1500 K, before cooling to 1200 K where we equilibrated longer. We then cooled the cluster down to 200 K, decreasing the temperature in intervals of 100 K. At each temperature the system is equilibrated for 5×10^6 steps (21.5 ns) using the Andersen thermostat method. With this cooling method we find that our cluster solidifies into an Ih structure¹¹.

In Fig. 9 we show an instantaneous configuration of this $N = 2624$ gold cluster at our lowest temperature, $T = 200$ K. To clarify the geometry of the cluster, we have calculated the local curvatures for each surface atom according to the method of Section II C 2, and in Fig. 9(a) we shade each atom according to the maximal local curvature; the greater the curvature, the darker the gray scale. Comparison with Fig. 1 strongly suggests that our cluster has an Ih structure. Large curvature regions correspond to edges and vertices, while low curvature regions are the flat $\{111\}$ facets of the fcc tetrahedra. Note that some vertices have low curvature; this is because these vertices have their top most atom missing, and so form a small locally flat region.

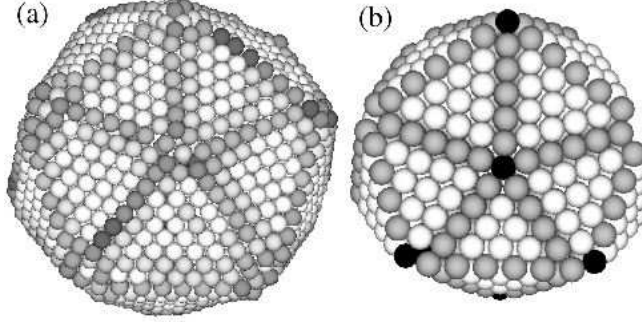


FIG. 9: Ih structure of an $N = 2624$ atom gold cluster at $T = 200$ K. (a) Surface of an instantaneous configuration with atoms shaded according to the maximal local curvature; the larger the curvature, the darker the gray scale. (b) The same configuration with the three outer most layers peeled away. Atoms are shaded according to their local crystal structure; white is fcc, gray is hcp, and black is “other”.

To further illustrate the Ih nature of our cluster, we have computed the local bond order parameters for each atom, averaging over all bonds that connect the given atom to its neighbors. Using the values in Table I, we then identify each atom with its local crystal structure. We regard atoms with $Q_4 > 0.15$ and $\hat{W}_4 \leq 0$ as having a local fcc structure, and atoms with $Q_4 \leq 0.15$ and $\hat{W}_4 > 0$ as having a local hcp structure; all other atoms are simply labeled as “other”. Because the surface layer and the two sub layers closest to the surface exhibit surface reconstruction and have frozen in surface fluctuations, we have peeled them away by use of the cone algorithm of Section II C 1. The resulting interior of the cluster is shown in Fig. 9(b), where fcc atoms are shaded white, hcp atoms gray, and “other” atoms black. The Ih structure of the cluster is readily apparent. One clearly sees the flat $\{111\}$ facets of the fcc tetrahedra, the edges of the facets corresponding to the hcp twin grain boundaries, and the vertices with 5-fold symmetry.

We have also applied the same cooling procedure on smaller gold clusters with $N = 603$ and $N = 1409$ atoms. In Fig. 10 we show the instantaneous configurations of $N = 603$ and $N = 1409$ at $T = 200$ K, with surface atoms shaded by their maximal local curvature (as was done in Fig. 9(a) for $N = 2624$). We again clearly see the Ih structure, however for the smaller cluster, the edges and facets appear slightly rounded.

It is interesting to note in Figs. 9 and 10 that the fcc tetrahedra of our clusters are not all of equal size. For a non-magic number N of atoms, such as is the case here, this is to

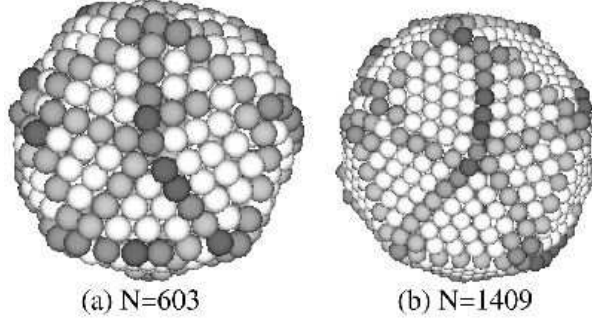


FIG. 10: Ih structure of gold clusters with (a) $N = 603$ and (b) $N = 1409$ atoms at $T = 200$ K. The atoms on the surfaces of these instantaneous configurations are shaded according to the maximal local curvature; the larger the curvature, the darker the gray scale.

be expected. However, we have also cooled clusters with magic numbers³⁹ $N = 560$ and $N = 1414$ from liquid to 200 K using the exact same cooling procedure. These clusters also formed asymmetric Ih structures with 20 facets of slightly unequal sizes. This suggests that our cooling procedure, while slow enough to balance surface vs. bulk free energy and find the Ih structures, is not slow enough to achieve the perfect global equilibration which one expects would result in perfectly symmetric structures for magic numbers N .

An interesting feature of our clusters that can not be seen in Figs. 9 and 10 is that all of our clusters formed with a missing central atom. The energetics of such vacancies at the center of Ih clusters were first considered by Boyer and Broughton⁴⁰ for Lennard-Jones clusters and later by Mottet *et al.*⁴¹ for Cu, Ag, and Au particles. Above a certain material dependent critical size the central vacancy lowers the energy of the cluster by partially releasing the strain caused by the mismatch of the tetrahedral units. Mottet *et al.* concluded that for gold particles the introduction of the central point defect does not lower the energy enough to make the icosahedron competitive with crystallographic octahedra and Wulff polyhedra. Their conclusion, however, was based solely on energy calculations which neglect the entropic contributions to the free energy at finite temperature. Our finite temperature simulations therefore suggest that such a constitutional vacancy can in fact stabilize icosahedral clusters of thousands of atoms, making them the observed structure upon cooling.

B. Melting and the bond orientational order parameters

Having determined that our clusters cooled from the liquid have the Ih structure, we then heated up the clusters using constant temperature MD instead of the Andersen thermostat, so that the total linear and angular momenta are conserved and vanish; this ensures that our clusters neither translate nor rotate during the course of our simulations. We heat in temperature intervals of 100 K when far from T_m , but use smaller intervals when approaching T_m . At each temperature the clusters have been equilibrated for 10^6 MD steps (4.3 ns), followed by 10^7 steps (43 ns) to collect data. Our simulation times are more than an order of magnitude longer than the ~ 1 ns typically simulated in earlier works^{6,7}.

In Fig. 11 we show the caloric curve (average potential energy per atom vs. temperature) for several of our cluster sizes, upon heating. The kink in each curve locates the cluster melting transition. Several expected trends²¹ are clearly seen: (i) the melting temperature increases as the cluster size increases, and (ii) the average potential energy per atom increases as the cluster size decreases, due to the larger surface-to-volume ratio. No qualitative difference is seen between the magic number sizes, $N = 922$ and 5082, and the others. Note that the glue model gives a melting temperature of 1357 K for bulk gold, well above that of our biggest cluster³⁰. The experimentally measured melting temperature of bulk gold is 1337 K⁴².

We have done our most careful heating for the $N = 2624$ atom cluster, taking fine temperature increments near T_m . Heating at the above rate of 43 ns per temperature, we find that the cluster has a first order melting transition at $T = 1075$ K. However, when we simulated the cluster at the slightly lower temperature of $T = 1070$ K for more than 240 ns, we found that it also ultimately melted. Thus the estimates of T_m from Fig. 11 are most likely slightly higher than the true equilibrium values. This superheating that we find is perhaps related to the extraordinary stability of the gold {111} surface, as was also observed in a slab-like geometry²⁰.

Next we wish to explore the melting transition from the perspective of the bond orientational order parameters, defined in Section II B. We are interested specifically to consider the behavior of the surface of the cluster as distinct from the behavior of the interior. We therefore use the cone algorithm recursively to group the atoms of the cluster into successive layers. The outer most layer of atoms is identified as the surface layer; the atoms immedi-

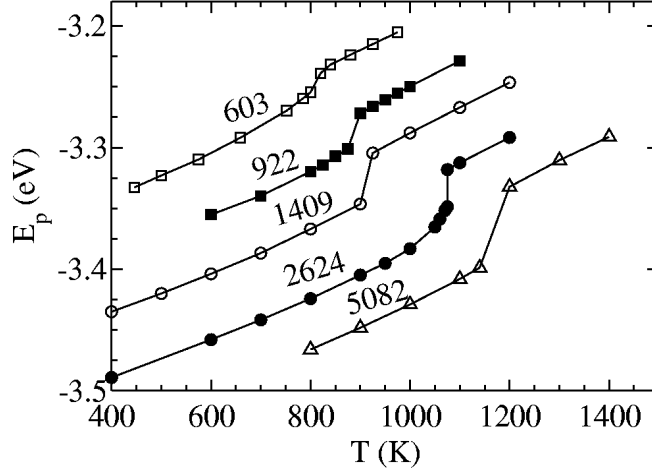


FIG. 11: Caloric curve of Ih gold clusters with $N = 603$, 1409, and 2624 atoms, as well as with magic numbers³⁹ of $N = 922$ and 5082 atoms.

TABLE II: Average numbers of atoms in the surface layer, the sub layers and the bulk of an $N = 2624$ atom gold cluster at different temperatures.

T	Surface	Sub layer 1	Sub layer 2	Sub layer 3	Sub layer 4	Bulk
400 K	858.5 ± 0.6	602.8 ± 0.8	428.3 ± 1.1	307.4 ± 1.1	207.2 ± 0.8	219.6 ± 1.1
600 K	859.8 ± 1.2	602.2 ± 1.4	427.9 ± 1.2	307.3 ± 1.1	207.2 ± 0.9	219.7 ± 1.1
900 K	867.7 ± 2.4	594.9 ± 2.6	427.5 ± 1.4	307.0 ± 1.2	207.0 ± 1.0	219.9 ± 1.1
1060 K	869.9 ± 3.6	582.4 ± 4.0	436.2 ± 3.2	311.3 ± 2.6	208.6 ± 2.2	215.7 ± 3.2
1100 K	874.7 ± 3.9	572.4 ± 4.2	436.2 ± 4.2	308.7 ± 4.0	209.9 ± 3.7	222.1 ± 5.1

ately below the surface layer are called the first sub layer, then the second sub layer, and so on. For the cluster of $N = 2624$ atoms there are a total of 9 such layers. We label the atoms lying below the fourth sub layer as “interior” or “bulk” atoms. For $N = 2624$, we show in Table II the number of atoms in each layer for various temperatures up through melting. What is immediately apparent is that as the temperature varies within the solid phase, $T < T_m \simeq 1075$ K, the number of atoms in a given layer remains essentially constant, within about ~ 5 , for all layers below the second sub layer. The surface and top two sub layers, however, display a more noticeable variation, suggesting changes on the surface of the cluster well below melting.

Having made this division into layers, we then compute the four bond orientational order

parameters Q_4 , Q_6 , \hat{W}_4 , and \hat{W}_6 , defined in Section II B, separately for each layer and for the bulk. In Fig. 12 we show our results for the $N = 2624$ atom cluster; Fig. 12(a) is for the interior atoms, while Fig. 12(b) is for the surface atoms. Comparing to the values listed in Table I, or equivalently as shown in Fig. 2, we see that the values we now find at low temperature are quite consistent with the bulk and surface values appropriate for an Ih structure. The only exception to this is the case of \hat{W}_4 which we find to be approximately zero, rather than the negative or positive number shown in Table I. However we have found that, unlike the other bond order parameters, the value of \hat{W}_4 is extremely sensitive to the symmetry of the perfect Ih structure. For deviations from this perfect structure, as is the case for our simulated cluster, \hat{W}_4 can vary dramatically. This is evidenced by the very large sample to sample fluctuations we found for \hat{W}_4 , as indicated by the very large error bars shown in Fig. 12 for \hat{W}_4 as compared to the other quantities. We thus conclude that the bond orientational order parameters are very consistent with our cluster being a Mackay icosahedron.

In Fig. 12(a) for the interior atoms, we see that bulk bond orientational order parameters remain roughly constant until just above 1000 K, before taking a sharp drop towards zero at the same melting temperature, $T_m \simeq 1075$ K, as found from the caloric curve of Fig. 11. Thus the bond orientational order parameters give a good signature of the melting transition. The sharp decrease of the bond parameters indicates that the interior atoms remain with a highly ordered Ih structure until just before melting. Note that the values in the liquid above T_m are not identically zero, but have small finite values due to the finite size of the liquid cluster; this effect is biggest for Q_6 .

In Fig. 12(b) for the surface atoms, we again see that the bond orientational order parameters remain with their Ih values at low temperatures, and then vanish towards zero at the *same* T_m as for the bulk atoms. Thus we reach one of our most important conclusions: the presence of finite surface bond orientational order up until the bulk melting transition indicates that the surface $\{111\}$ facets of the Ih structure do *not* premelt, but rather *the surface facets melt at the same temperature as the bulk*. The absence of any sharp features in the surface bond orientational order parameters below T_m suggests that there are no other types of surface phase transitions below T_m . There is, however, one noticeable difference in the behavior of the surface bond orientational order parameters as compared to the bulk. We see that the surface parameter Q_6 starts a noticeable decrease from its low temperature

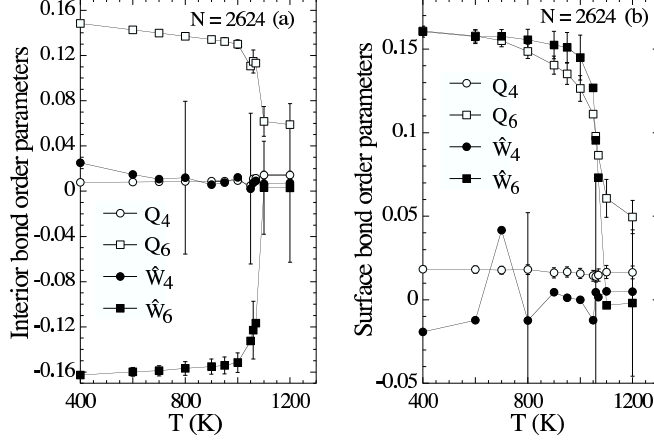


FIG. 12: Bond orientational order parameters of the $N = 2624$ atom cluster for (a) the interior atoms, and (b) the surface atoms. Sample error bars, representing configuration to configuration fluctuations, are shown.

value at $T \sim 800$ K, considerably below the melting T_m . We interpret this as a softening of the surface, and we will present the reason for this behavior in the following section.

We have also measured the bond orientational order parameters for the first through fourth sub layers of the cluster. Since Q_6 is the bond parameter that most clearly shows the surface softening, in Fig. 13 we plot the value of Q_6 vs. temperature, for surface, interior, and each of the four sub layers. Since each layer has a slightly different value of Q_6 at low temperature, we plot the normalized values $Q_6(T)/Q_6(400 \text{ K})$ so as to better compare their relative behaviors. We see that both the surface and the first sub layer show almost identical softening as T_m is approached. However all the deeper sub layers show almost identical behavior as the interior atoms, with almost no softening until T_m . Thus the softening phenomenon is seen to be largely confined to the top two layers of the cluster and does not propagate more deeply as T_m is approached; below the top two layers, the cluster remains almost as ordered as at low temperatures, until just before melting.

We have also tested the sensitivity of our definition of the “interior” atoms of the cluster, by redefining it to be *all* the atoms below the surface layer. However, as might be expected from Fig. 13, computing the bulk bond orientational order parameters defined this way gives no qualitative change from the behavior seen in Fig. 12(a).

In Figs. 14 to 17 we show similar plots of interior and surface bond orientational order parameters for our other cluster sizes, $N = 603, 922, 1409$ and 5082 . We see the same

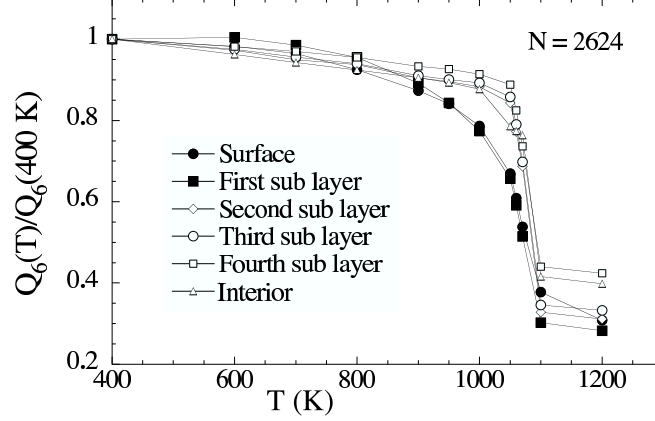


FIG. 13: Normalized bond orientational order parameter $Q_6(T)/Q_6(400 \text{ K})$ for the surface, interior, and various sub layers of the $N = 2624$ atom cluster.

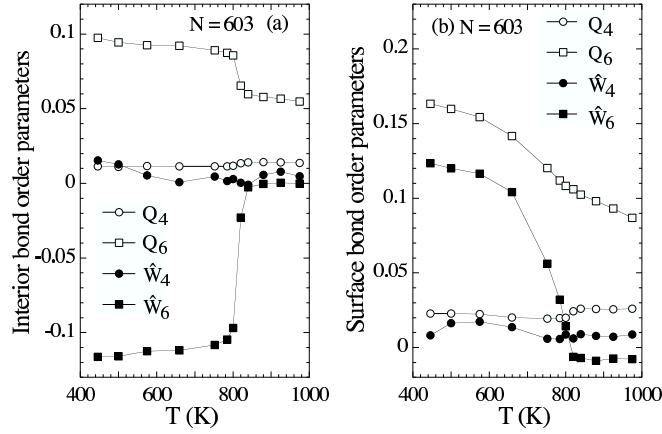


FIG. 14: Bond orientational order parameters of the $N = 603$ atom cluster for (a) the interior atoms, and (b) the surface atoms.

qualitative behaviors as in Fig. 12, with surface and bulk melting at the same temperature. This melting temperature, which increases with cluster size, agrees with the values found from the caloric curves of Fig. 11. Surface *softening* tracks the melting temperature and starts to be noticeable about 200 K below T_m . The surface softening is somewhat enhanced for the smaller cluster sizes. There appears to be no qualitative differences for our magic number³⁹ clusters, $N = 922$ and 5082, as compared to the other sizes.

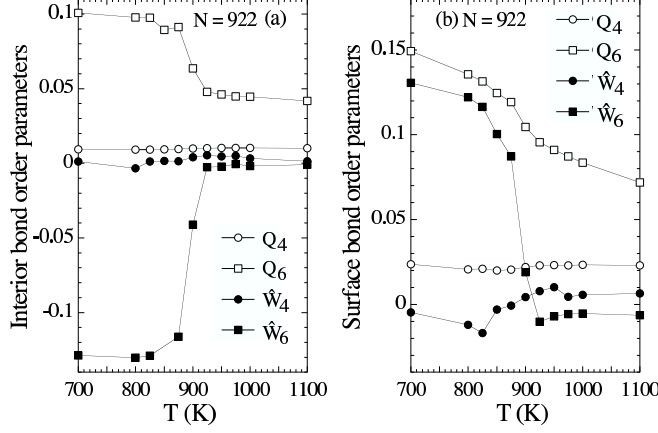


FIG. 15: Bond orientational order parameters of the magic number $N = 922$ atom cluster for (a) the interior atoms, and (b) the surface atoms.

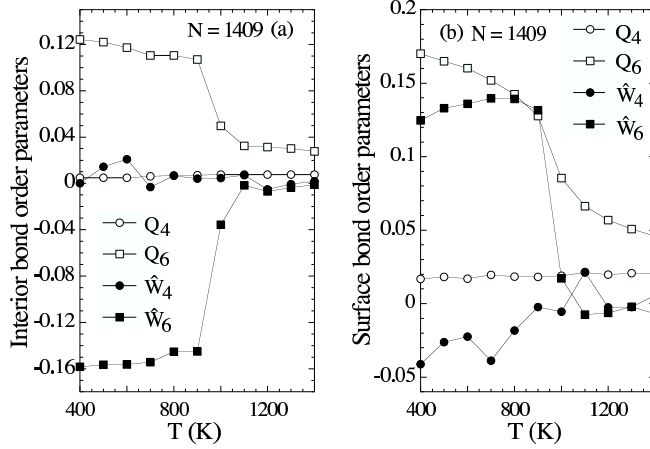


FIG. 16: Bond orientational order parameters of the $N = 1409$ atom cluster for (a) the interior atoms, and (b) the surface atoms.

C. Average shape and surface curvature

To understand the physical manifestations of the surface softening that is indicated by the surface bond orientational order parameters, we now look at the average shapes of our cluster, computed according to the method of Section II C 3. We focus first on our cluster of $N = 2624$ atoms. For this case, we have divided the 4π total solid angle into 842 almost equal solid angles, using the icosahedral covering of Ref. 37. We have chosen this number since it corresponds as close as possible to the typical number of surface atoms in the cluster (see Table II). At each temperature over 1000 instantaneous configurations,

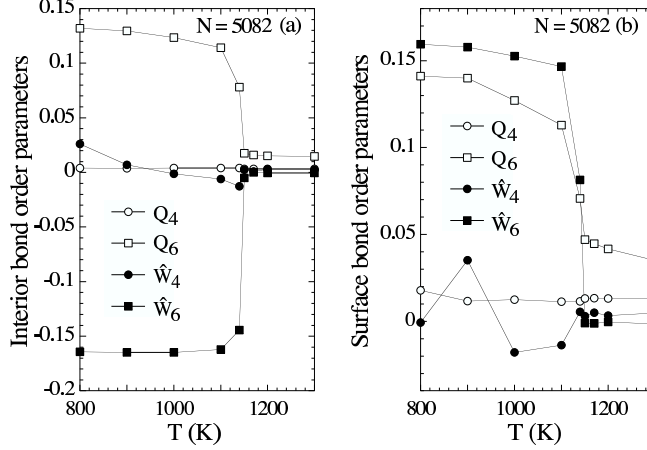


FIG. 17: Bond orientational order parameters of the magic number $N = 5082$ atom cluster for (a) the interior atoms, and (b) the surface atoms.

sampled at equal intervals throughout the simulated time of 43 ns, have been included in our average. We show the resulting average shapes in Fig. 18. We present results for the following temperatures: 400 K, representing the low temperature configuration in which thermal fluctuations are negligible; 600 K where one starts to notice small changes in the surface; 900 K where substantial softening of the surface orientational order parameter Q_6 is observed; 1060 K, just below the melting $T_m \simeq 1075$ K; and $T = 1100$ K just above T_m .

In the top row of Fig. 18 we show pictures constructed similarly to that in Fig. 8(c) of Section II C 3, which showed the average shape of the liquid cluster at $T = 1200$ K. The small spheres represent the average position of the surface within the given solid angle. Additionally, we have now shaded these spheres according to the value of the maximal local surface curvature, as we did earlier in Fig. 9(a) for an instantaneous configuration at $T = 200$ K; the darker the gray scale, the larger the curvature. This method of shading is used to highlight any edges and facets that are on the cluster surface. The view point for these pictures is taken at infinity, so as to show a full hemisphere of solid angle.

In the bottom row of Fig. 18 we show the corresponding average shapes using a smooth 3D contour plot with overhead lighting. The view point for these bottom row pictures is now taken to be a finite distance from the cluster, in order to highlight the straight edges and 5-fold symmetry about the vertices.

The pictures in Fig. 18 illustrate the following scenario as the cluster is heated. At low temperatures the cluster is almost fully faceted, with flat facets meeting at sharp edges and

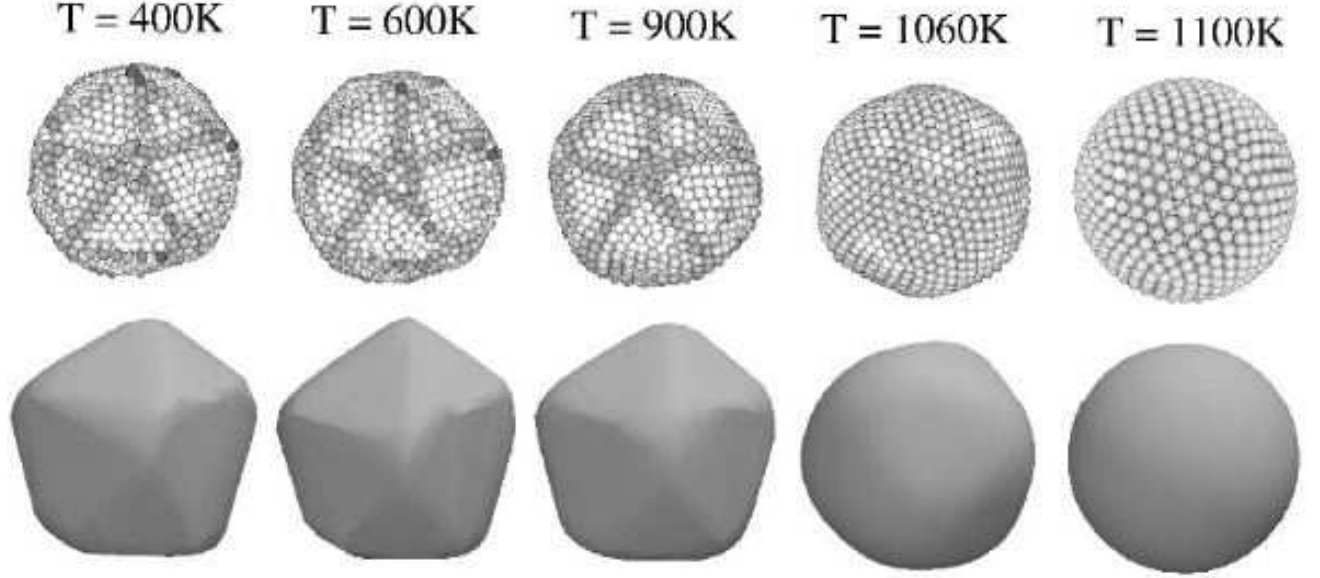


FIG. 18: Average shapes of an $N = 2624$ atom cluster at 400, 600, 900, 1060 and 1100 K. The top row shows each of the discretized solid angles of the surface shaded according to the value of the maximal local curvature; the darker the gray scale, the larger the curvature. The viewpoint of these pictures is set to infinity, to show a full hemisphere of solid angle. The bottom row is the corresponding smooth contour plot, with a finite viewpoint so as to highlight the straight edges and 5-fold symmetry about the vertices.

vertices. By 900 K the facets have shrunk slightly in size and the edges and vertices have noticeably rounded. At 1060 K, just below melting, the facets have shrunk to almost negligible size, and the cluster is almost spherical. Above melting, the cluster is essentially a perfect sphere.

As a way to quantify the cluster shapes we have computed the bond curvatures c_b and the maximal local surface curvatures κ_M , as defined in Section II C 2. In Figs. 19(a)-(d) we show histograms of bond curvature c_b for the four temperatures 600, 900, 1060 and 1100 K. The solid curves show the histograms of bond curvatures as computed over the surface bonds of the *average* cluster shape shown in Fig. 18. In contrast, the dashed curves show the histograms of bond curvatures computed for an *instantaneous* cluster configuration, and then averaged over the 1000 instantaneous configurations saved in our simulated time of 43 ns. Note that for the histograms for the average shape, where since we are dealing with only

one average configuration we have relatively few points in our histogram, we have smoothed our data using a Gaussian smoothing function with a width of 4 bins. The bin size here is 0.006 \AA^{-1} . In Figs. 20(a)-(d) we show the analogous histograms for the maximal local curvature κ_M . The bin size here is 0.02 \AA^{-1} . Note that κ_M can be negative, corresponding to a region where the surface is locally concave; an example of when this can happen is near a vertex which is missing its top most atom.

Both Figs. 19 and 20 illustrate the same scenario. Consider first the histograms of the average cluster shapes. At low temperatures, the histograms show a strong peak at zero, representing the low curvatures of the large flat facets. The histograms also show either a second peak or plateau at higher curvature, with a long high curvature tail, representing the large curvatures at edges and vertices. We can compare these results against those in Fig. 7 for the ideal Ih structure. In the liquid above $T_m \simeq 1075 \text{ K}$, the histograms have a single sharp peak at finite curvature, representing the uniform curvature of the spherical liquid cluster. Just below melting, at $T = 1060 \text{ K}$, the histograms similarly show a single peak near that of the liquid, only noticeably broader than for the liquid; this indicates the shrinkage of the flat facets to negligible size and a rounded cluster that is not yet a perfect sphere.

Comparing the histograms for the average vs. the instantaneous shapes, the latter are in general broader, most especially for the liquid cluster. This demonstrates the presence of strong thermal shape fluctuations about the average shape. Particularly interesting are the histograms for 1060 K , just below T_m , in Figs. 19(c) and 20(c), and for 1100 K , just above T_m , in Figs. 19(d) and 20(d). The histograms for the average shape are symmetric Gaussian like peaks about an average curvature, corresponding to a spherical or nearly spherical cluster. The histograms for the instantaneous configurations, however, are skewed in shape. They have a low curvature peak and a broad high curvature tail, somewhat similar to what is seen at lower temperatures. This suggests that the instantaneous configurations can still develop small local facets on the surface. A similar observation has previously been made by Lewis *et al.* for smaller clusters²². Fluctuations of the edges and vertices of these local facets lead to an effective diffusion of the facet upon the cluster surface; averaging over these fluctuations results in a smoothing out of the facets to negligible size when one considers the *average*, rather than the instantaneous, cluster shape. We have seen evidence for this scenario by visual inspection of instantaneous cluster configurations. For example, in the instantaneous

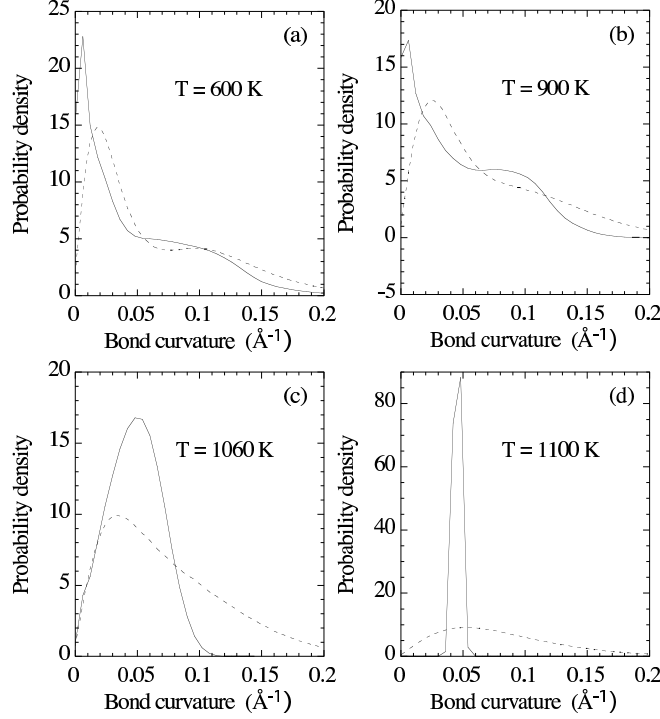


FIG. 19: Histograms of bond curvature c_b for the average cluster shape (solid lines) and the instantaneous cluster configurations (dashed lines) at (a) $T = 600$ K, (b) $T = 900$ K, (c) $T = 1060$ K, and (d) $T = 1100$ K. The cluster size is $N = 2624$ atoms.

liquid cluster configuration shown in Fig. 8(b) one clearly sees a flat edge along the bottom.

For comparison with other sizes, we show in Fig. 21 average cluster shapes for our $N = 1409$ atom cluster at temperatures 800 K and 900 K, where $T_m \simeq 925$ K. In Fig. 22 we show average shapes for our magic number³⁹ $N = 5082$ atom cluster at temperatures 1000 K and 1140 K, where now $T_m \simeq 1150$ K. The gray scale in these figures is the same as used in Fig. 18. Again we see facets shrinking, and the cluster becoming more spherical, as T_m is approached.

D. Diffusion of atoms

In this section we present further evidence that the physical mechanism behind the surface softening is indeed the diffusion of atoms on the vertices and edges of the cluster. We will consider in this section only the cluster of $N = 2624$ atoms.

We start by first considering the *inter*-layer mixing of atoms in the cluster, defining an

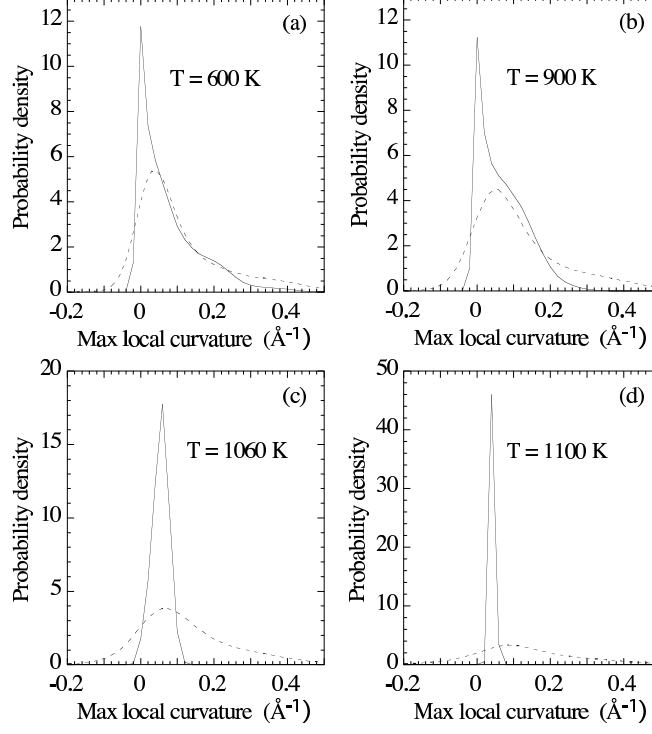


FIG. 20: Histograms of maximal surface curvature κ_M of the average cluster shape (solid lines) and the instantaneous cluster configurations (dashed lines) at (a) $T = 600\text{K}$, (b) $T = 900\text{ K}$, (c) $T = 1060\text{ K}$, and (d) $T = 1100\text{ K}$. The cluster size is $N = 2624$ atoms.

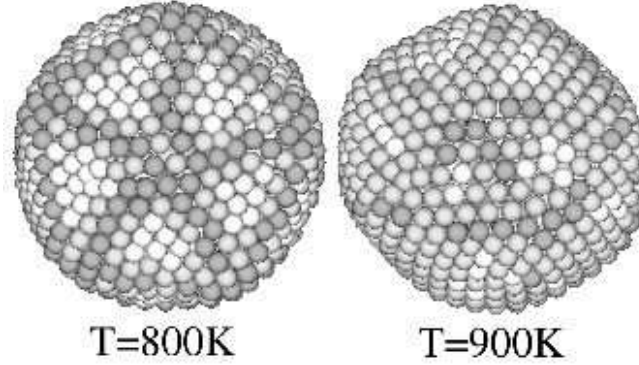


FIG. 21: Average cluster shapes for an $N = 1409$ atom cluster at temperatures 800 K and 900 K , where $T_m \simeq 925\text{ K}$.

inter-layer mixing parameter $\langle n \rangle$ as follows. At each temperature we label the atoms in the initial configuration by an integer $n' = 0, 1, 2, \dots, 5$ according to whether the atom is on the surface, in the first sub layer, second sub layer, \dots , or interior of the cluster. At the end of the simulation for that temperature, we assign a new integer n to each atom, according to which

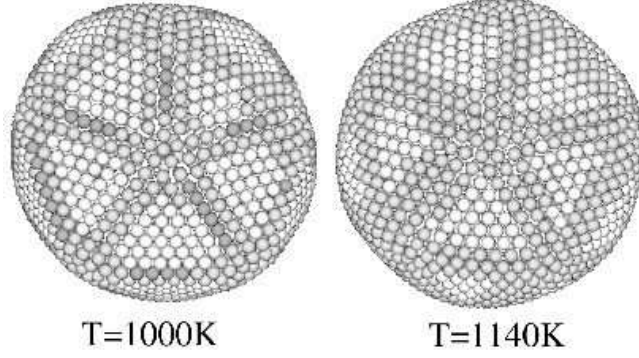


FIG. 22: Average cluster shapes for an $N = 5082$ atom cluster at temperatures 1000 K and 1140 K, where $T_m \simeq 1150$ K.

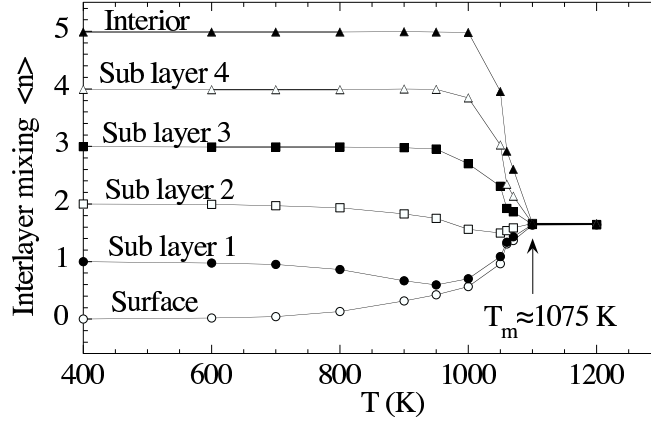


FIG. 23: Interlayer mixing parameter $\langle n \rangle$ vs. T , for atoms initially on the surface, in the first sub layer, \dots , and in the interior. The cluster size is $N = 2624$ atoms.

layer the atom is now in. In Fig. 23 we plot $\langle n \rangle$ vs. T , where n is averaged separately over each group of atoms indexed by their initial layer number n' . When $\langle n \rangle$ differs noticeably from the initial n' , it indicates significant inter-layer mixing of the atoms from layer n' into other layers. From Fig. 23 we see that noticeable inter-layer mixing takes place between the surface and the first sub layer as low as 700 K; these two layers are almost evenly mixed by 950 K, more than 100 K below the melting $T_m \simeq 1075$ K. As T_m is approached, additional layers start to mix together. At T_m and above, all layers are evenly mixed during the course of the simulation, indicating that in the liquid all atoms diffuse equally throughout the entire cluster.

Next we consider the diffusion of the atoms in the cluster by computing the mean squared displacements, $\Delta r^2(t)$, defined in Eq. (16). We compute $\Delta r^2(t)$ separately for each layer of

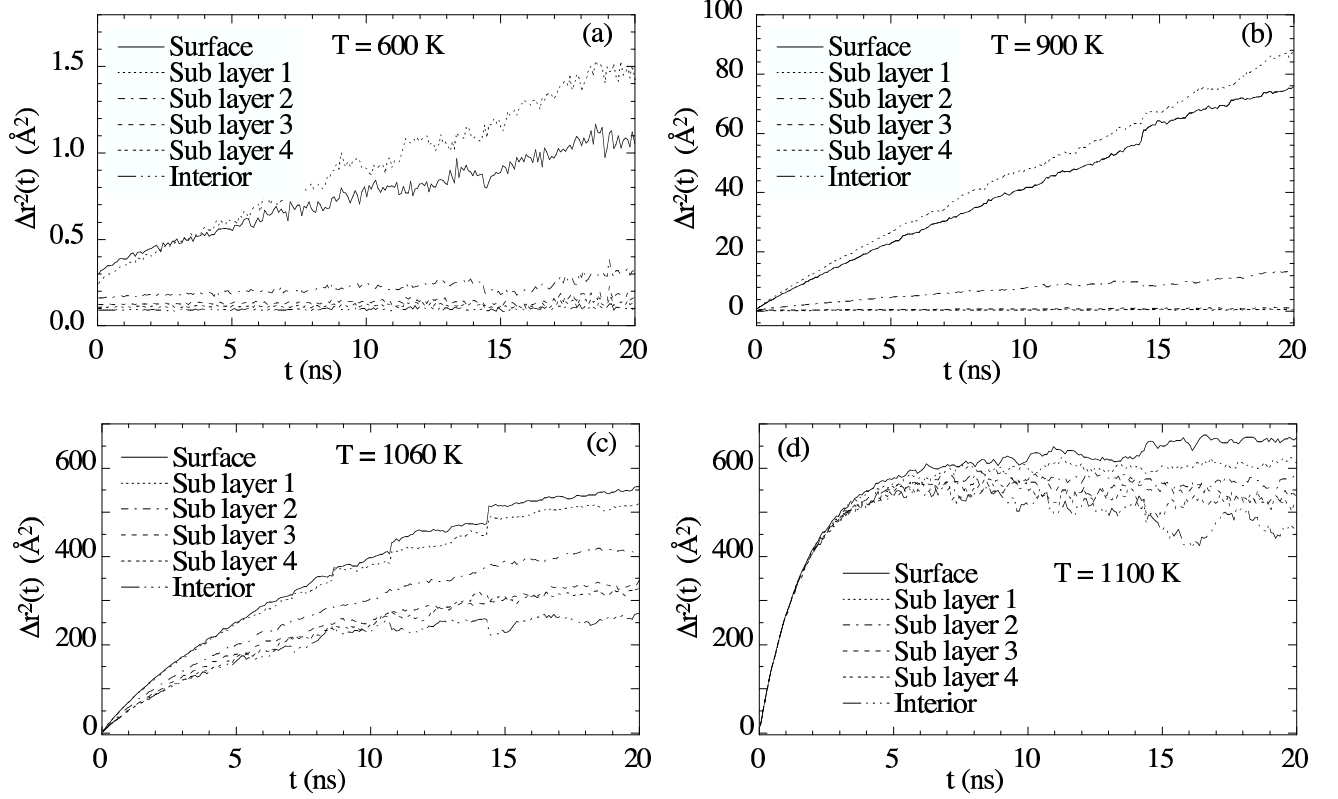


FIG. 24: Mean squared displacements for the $N = 2624$ atom cluster averaged over the atoms in the surface layer, first through fourth sub layers, and interior for (a) 600 K, (b) 900 K, (c) 1060 K, and (d) 1100 K.

the cluster (and the interior) by averaging only over the atoms that are *initially* in a given layer. In Figs. 24(a)-(d) we plot our results for $\Delta r^2(t)$ vs. t , layer by layer, for the four different temperatures, 600, 900, 1060 and 1100 K. Note that since atoms in different layers can mix (see Fig. 23), the division into different layers in Fig. 24 contains some ambiguity; an atom initially in the first sub layer, for example, might during the course of the simulation wind up on the surface, however we continue to average its motion in with that of the first sub layer.

Several expected features are apparent in Fig. 24. In Fig. 24(d) at 1100 K, above the melting $T_m \simeq 1075$ K, we see that all layers behave roughly the same, saturating at $\Delta r^2 \sim 600 \text{ \AA}^2$. This is consistent with a liquid cluster of radius $\sim 21 \text{ \AA}$, in which all the atoms can diffuse throughout the entire cluster, no matter which layer they were initially in. At the low temperature of 600 K, where the average cluster shape remains almost fully faceted, the results in Fig. 24(a) show that diffusion is almost negligible. Even for the two top layers,

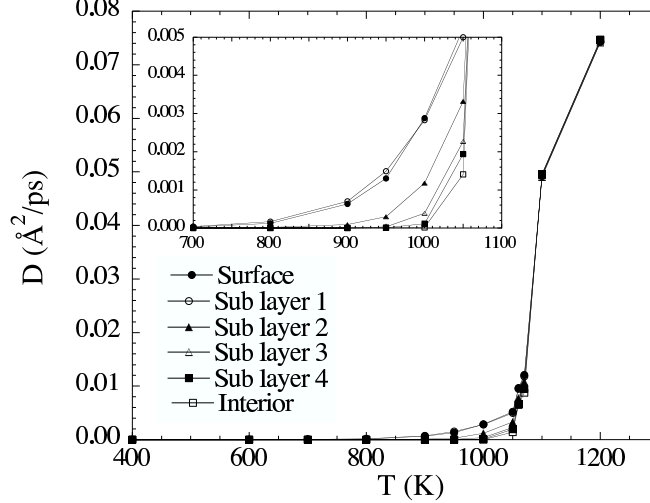


FIG. 25: Diffusion coefficients D vs. T for different layers of the $N = 2624$ atom cluster. The inset shows an expanded range for D in a temperature range below melting, 700 – 1050 K.

atoms on average move less than one inter-atomic spacing ($\sim 3 \text{ \AA}$) over the observation time of 20 ns. At 900 K, where the edges and vertices of the average cluster shape have noticeably rounded, we see in Fig. 24(b) that diffusion in the top two layers is significant, with atoms on average traveling a root mean square distance equal to several inter-atomic spacings. The second sub layer also shows a noticeable diffusion but all more inward atoms diffuse negligibly. At 1060 K, just below the melting $T_m \simeq 1075 \text{ K}$, we see that all atoms are diffusing a significant amount throughout the cluster, with the top two layers almost reaching the long time saturation value $\sim 600 \text{ \AA}^2$ found in the liquid.

In Fig. 25 we plot the diffusion constant D vs. T for each of the cluster layers, obtained by fitting to the early time linear part of the curves in Fig. 24. If we fit our diffusion constant for the surface layer to the simple form $D = D_0 \exp(-E_A/k_B T)$ to extract the activation energy, $E_A = -d(\ln D)/d(1/k_B T)$, we find the values of $E_A = 0.21 \text{ eV}$ at low temperatures, $\sim 500 \text{ K}$, where the cluster is fully faceted. At high temperature, $\sim 1200 \text{ K}$, in the liquid, we find $E_A = 0.35 \text{ eV}$. Note that the first value corresponds to surface diffusion, while the second value corresponds to *bulk* diffusion in the liquid (since once the cluster has melted, atoms initially on the surface easily diffuse into the bulk). To compare with previous simulations, Boisvert et al.⁴³ did a first principles calculation for the gold $\{111\}$ surface at low temperatures and found $E_A = 0.22 \pm 0.03 \text{ eV}$, in good agreement with our value. Chushak and Bartell⁷ reported the value of $E_A = 0.25 \text{ eV}$ using the EAM model

for a liquid gold nanocluster. Considering the tendency of the EAM model to systematically give lower energy values (as pointed out in Ref. 44), our result for the liquid is in reasonable agreement.

A seeming paradox concerning our diffusion results of Fig. 24 is that at low temperatures the diffusion of atoms in the first sub layer appears to be greater than that for atoms on the surface. This can be explained by noting that the Δr^2 in Fig. 24 represent an *average* over *all* the atoms in a given layer. As we will show below, at low temperatures, atoms along the edges and on the vertices of a given layer are more mobile than a typical atom in that layer. Since the fraction of such edge and vertex atoms is larger in the first sub surface layer than on the surface, atoms in this layer have a larger average mobility. When the temperature increases to 1060 K, most of the atoms in the two layers are now diffusing, and the average mean squared displacements Δr^2 of the two layers become roughly equal.

A more serious issue is how to reconcile our results of Fig. 24, showing noticeable surface diffusion below T_m , with our claim that the surface $\{111\}$ facets remain ordered and do not premelt below T_m , as indicated from the finite values of the bond orientational order parameters shown in Fig. 12(b). One possibility is that the surface layer does in fact melt at a well defined temperature below T_m , but that orientational order in the liquid surface is maintained due to the presence of an effective periodic substrate formed by the ordered sub layers below the surface. However we do not believe that this is the case. Even if orientational order in a liquid surface were preserved by the presence of the ordered sub layers, one would still expect to see some kink or other feature in the bond orientational order parameters at the surface melting transition. In contrast, we find in Fig. 12b that the bond order parameters go smoothly, though near T_m steeply, to zero. Instead of the above scenario, we believe that the surface diffusion that we observe below T_m is due not to atoms on the $\{111\}$ facets, but rather due to the atoms along the vertices and edges of the surface. As temperature increases, the facets shrink in size, the edges get rounder and broader, and the effective number of such diffusing atoms increases. Just below T_m the facets have shrunk to almost negligible size, the bond order parameters have decreased to a corresponding small but finite value, and most of the atoms on the surface are now diffusing.

To estimate the number of atoms in each layer that are diffusing, we use the following criterion. We compute the number of atoms in each layer that have moved a distance of more than 8 Å within 20 ns of simulated time. The cutoff of 8 Å is chosen since it

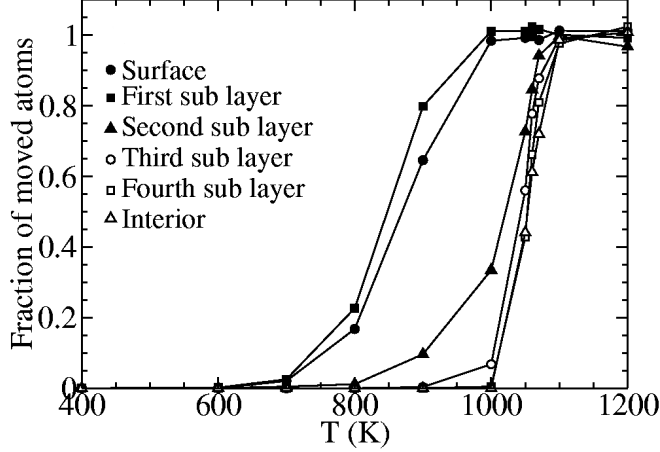


FIG. 26: Fraction of atoms per layer that have moved more than 8 Å from their initial position, in 20 ns, for the $N = 2624$ atom cluster.

is the distance between the third and fourth peak of the pair correlation function, thus representing a distance roughly between the third and fourth nearest neighbor; we assume that an atom which can move this far is in fact diffusing, rather than just undergoing thermal motion about a fixed average position. We find our results to be qualitatively insensitive to choosing a smaller cutoff length of 6 Å (the distance between the second and third peaks of the pair correlation function). In Fig. 26 we plot the fraction of such “moved” atoms vs. temperature, for the surface, sub layers, and interior of the cluster. We see that only the surface and the first sub layer have a significant fraction of moved atoms below melting. This fraction steadily increases with temperature, and approaches unity at $T \sim 1000$ K, just below T_m . We interpret the unmoved fraction as those atoms on the ordered $\{111\}$ facets, which shrink in size as T approaches T_m . Close enough to T_m , when the facets become so small that they are only a few atoms across, it becomes easy for atoms on or near the edge of a facet to exchange with mobile atoms in the surrounding “liquid” of edge atoms; hence even such facet atoms can ultimately diffuse throughout the cluster, and the fraction of moved atoms can approach unity below T_m . Indeed the concept of liquid vs. solid become somewhat ambiguous when referring to such small surface areas as the $\{111\}$ facets just below T_m .

Combining all the above we infer the following scenario for diffusion at low temperatures: only atoms on the surface and in the first sub layer show any noticeable diffusion well below T_m . The atoms in these two layers that diffuse are the same atoms which mix between

the two layers (see Fig. 23), and these are the atoms along the edges and vertices of each layer. The atoms from the first sub layer diffuse by migrating first to the surface, and then diffusing upon the surface, until mixing back into the first sub layer. As the temperature increases to T_m , the facets shrink and the number of diffusing edge atoms increases, until all surface atoms are diffusing just below T_m .

To substantiate the above picture, we plot in Fig. 27 the displacement ellipsoids, defined in Section II D, for all atoms initially on the surface of our $N = 2624$ cluster. We show results for temperatures 400, 600, 900, 1060 and 1100 K, corresponding to the same temperatures for which we showed the average cluster shape in Fig. 18. In the top row we show ellipsoids averaged over a simulated time of 1.075 ns. We expect that atoms which are diffusing, with $\Delta r^2 \sim t$, should have their displacement ellipsoid roughly double in size when the time interval goes up by a factor of four. Hence in the bottom row of Fig. 27 we then show results for a simulated time of 4.3 ns, i.e. four times longer than the top row. We observe the following. At 400 K there is no observable diffusion of surface atoms. At 600 K we see diffusion of atoms at the vertices of the Ih cluster. At 900 K we see stronger diffusion at the vertices, as well as diffusion along the edges. One also can see several of the ellipsoids oriented normal to the surface, indicating atoms which are mixing in with the first sub layer. Atoms at the centers of the facets remain without diffusion. At 1060 K and above most of the atoms are clearly diffusing.

IV. DISCUSSION AND CONCLUSIONS

We have carried out long time equilibrium molecular dynamics simulations to study the behavior of gold nanoclusters cooled from the liquid, and their subsequent melting upon reheating. For three different generic cluster sizes, $N = 603$, 1409, and 2624, we found that the cooled clusters formed a slightly asymmetric Mackay icosahedral (Ih) structure with a missing central atom.

Using the above clusters cooled from the melt, as well as several other “magic number” Mackay icosahedra with up to $N = 5082$ atoms that we constructed by hand³⁹ at low temperature, we slowly heated these clusters up through melting. Measuring surface and bulk bond orientational order parameters we find a sharp cluster melting transition at a

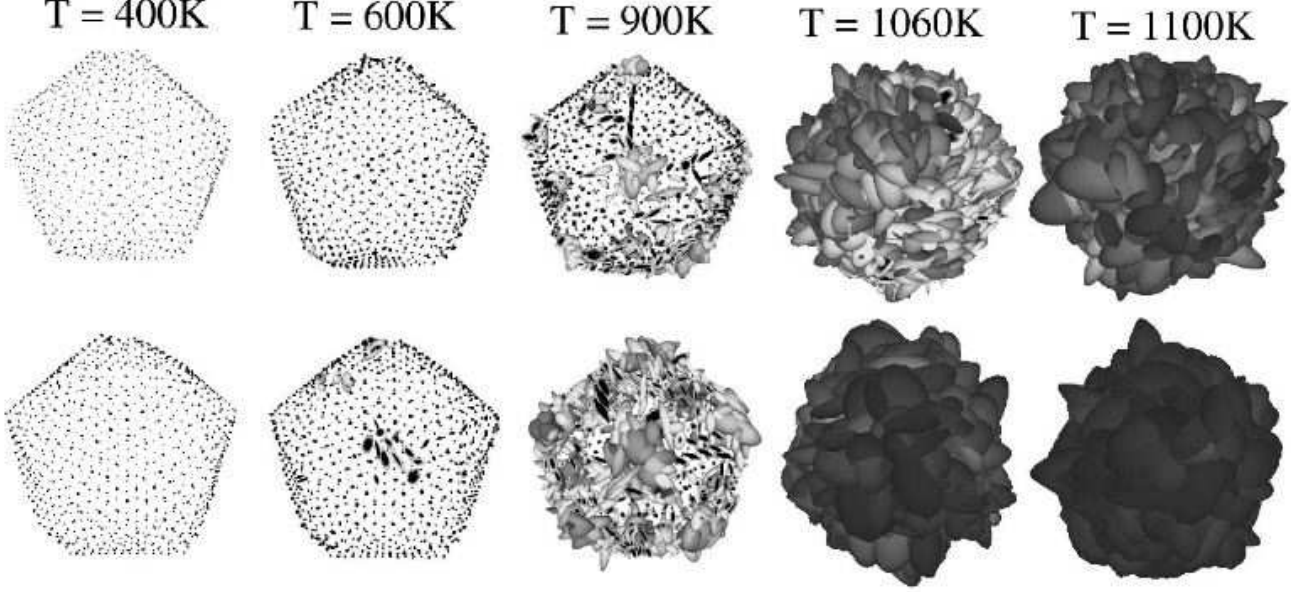


FIG. 27: Ellipsoids of displacement at 400, 600, 900, 1060 and 1100 K for the cluster of $N = 2624$ atoms. Each ellipsoid is centered at the average position of the given atom, and shows the directional distribution of root mean squared displacements. The top row gives results obtained for a simulated time of 1.075 ns, while the bottom row is for 4.3 ns.

temperature $T_m(N)$ that increases with cluster size, and that the $\{111\}$ facets on the surface do not premelt but remain ordered up until T_m . The surface bond parameters however decrease from their perfect Ih values significantly below T , indicating a softening of the surface prior to melting. We find that the onset of this surface softening appears to track the size dependent melting, occurring roughly 200 K below $T_m(N)$.

Looking at the average shape of our clusters, we see that this surface softening corresponds to a rounding of the edges and vertices of the cluster, with a corresponding shrinkage of the $\{111\}$ facet area. Just below the melting T_m the average cluster shape is nearly spherical. As the temperature increases towards melting, and in the liquid above T_m , instantaneous cluster configurations can display large thermal fluctuations about this average shape.

Measuring the diffusion of atoms in the cluster, we conclude that the mechanism for this surface softening is the onset of diffusion of atoms at first the vertices and then the edges of the cluster surface, as temperature is increased. As temperature further increases, the mobility of these atoms increases, and more and more atoms near the edges of the facets participate in this diffusion, until the number of atoms remaining stationary on the facets

becomes almost negligibly small near T_m . Simultaneous with this increasing diffusion is an increase in interlayer mixing, with surface and first sub layers mixing first, and then deeper layers mixing in as one approaches close to T_m .

A similar rounding of edges and shrinking of facets occur in the theory of the equilibrium shape of macroscopically large crystals, where the continuum Wulff construction⁴⁵ can be applied. In this theory, the shrinkage of facets is associated with approaching a roughening transition of the faceted surface, and the facet length shrinks proportionally to the inverse of the roughening correlation length⁴⁶. We do not believe that this theory explains the results for our clusters. Firstly, it is generally believed^{18,19} that the $\{111\}$ gold surface that forms the facets of our cluster does not have a roughening transition below the bulk melting transition. This is consistent with our observation that the surface softening of our clusters seems to track the size dependent cluster melting temperature rather than approaching a size independent onset temperature as would be expected if there was a true thermodynamic roughening transition. Moreover, the vanishing of facets at the roughening transition occurs within the context of the crystalline state; no diffusion of atoms need be involved. In our case it is clear that diffusion of atoms along the vertices and edges plays an important role. We therefore believe that the phenomena we observe in our simulated nanoclusters are due specifically to the finite, relatively small, size of our clusters, for which continuum approaches are not valid and one must consider the atomistic nature of the system. The rounding of edges and shrinkage of facets that we observe are better attributed to a “melting” of the cluster edges, which then spreads out into the ordered facets as the temperature increases towards melting.

V. ACKNOWLEDGMENT

This work was funded in part by DOE grant DE-FG02-89ER14017.

¹ J. Zheng, Z. Chen, and Z. Liu, *Langmuir* **16**, 9673 (2000).

² A. T. Bell, *Science* **299**, 1688 (2003).

³ Y. Xiao, F. Patolsky, E. Katz, J. F. Hainfeld, and I. Willner, *Science* **299**, 1877 (2003).

⁴ S. O. Obare, R. E. Hollowell, and C. J. Murphy, *Langmuir* **18**, 10 407 (2002).

- ⁵ S. Iijima and T. Ichihashi, *Phys. Rev. Lett.* **56**, 616 (1986).
- ⁶ C. L. Cleveland, W. D. Luedtke, and U. Landman, *Phys. Rev. B* **60**, 5065 (1999).
- ⁷ Y. G. Chushak and L. S. Bartell, *J. Phys. Chem. B* **105**, 11 605 (2001).
- ⁸ H.-S. Nam, Nong M. Hwang, B. D. Yu, and J.-K. Yoon, *Phys. Rev. Lett.* **89**, 275502 (2002).
- ⁹ L. D. Marks, *Rep. Prog. Phys.* **57**, 603 (1994).
- ¹⁰ J. A. Ascencio, C. Gutiérrez-Wing, M. E. Espinosa, M. Martín, S. Tehuacanero, C. Zorrilla, and M. José-Yacamán *Surf. Sci.* **396**, 349 (1998).
- ¹¹ A. L. Mackay, *Acta Cryst.* **15**, 916 (1962).
- ¹² T. P. Martin, *Phys. Rep.* **273**, 199 (1996). Note that this paper defines the central atom as $L = 1$, whereas in our Eq. (1) we take the central atom as $L = 0$.
- ¹³ S. Ino, *J. Phys. Soc. Japan* **27**, 941 (1969).
- ¹⁴ L. D. Marks, *Phil. Mag.* **49**, 81 (1984).
- ¹⁵ C. L. Cleveland, U. Landman, M. N. Shafigullin, P. W. Stephens, and R. L. Whetten, *Z. Phys. D* **40**, 503 (1997).
- ¹⁶ C. L. Cleveland, U. Landman, T. G. Schaaff, M. N. Shafigullin, P. W. Stephens, and R. L. Whetten, *Phys. Rev. Lett.* **79**, 1873 (1997).
- ¹⁷ K. Michaelian, N. Rendon, and I. L. Garzon, *Phys. Rev. B* **60**, 2000 (1999).
- ¹⁸ P. Carnevali, F. Ercolessi, and E. Tosatti, *Phys. Rev. B* **36**, 6701 (1987).
- ¹⁹ K. D. Stock and B. Grosser, *J. Cryst. Growth* **50**, 485 (1980).
- ²⁰ F. D. Di Tolla, E. Tosatti, and F. Ercolessi, *Interplay of melting, wetting, overheating and faceting on metal surfaces: theory and simulation*, in *Monte Carlo and molecular dynamics of condensed matter systems*, K. Binder and G. Ciccotti (Eds.), Società Italiana di Fisica, Bologna, 1996, p. 345-398.
- ²¹ F. Ercolessi, W. Andreoni, and E. Tosatti, *Phys. Rev. Lett.* **66**, 911 (1991).
- ²² L. J. Lewis, P. Jensen, and J.-L. Barrat, *Phys. Rev. B* **56**, 2248 (1997).
- ²³ Y. Wang, S. Teitel, and C. Dellago, *Chem. Phys. Lett.* **394**, 257 (2004).
- ²⁴ D. Marx and J. Hutter, *Ab initio molecular dynamics: Theory and implementation; Modern Methods and Algorithms of Quantum Chemistry*, J. Grotendorst (Ed.), Forschungszentrum Juelich, NIC Series, Vol. 1, 2000.
- ²⁵ S. M. Foiles, M. I. Baskes, and M. S. Daw, *Phys. Rev. B* **33**, 7983 (1986).
- ²⁶ J. N. Murrell and R. E. Mottram, *Mol. Phys.* **69**, 571 (1990).

- ²⁷ D. J. Wales and J. P. K. Doye, *J. Phys. Chem. A* **101**, 5111 (1997).
- ²⁸ J. P. K. Doye and D. J. Wales, *J. Chem. Soc. Farad. Trans.* **93**, 4233 (1997).
- ²⁹ I. L. Garzon and J. Jellinek, *Z. Phys. D* **20**, 235 (1991).
- ³⁰ F. Ercolessi, M. Parrinello, and E. Tosatti, *Philos. Mag. A* **58**, 213 (1988).
- ³¹ D. Frenkel and B. Smit, *Understanding Molecular Simulation: From Algorithms to Applications*, Academic Press: San Diego, 2002.
- ³² M. P. Allen and D. J. Tildesley, *Computer Simulation of Liquids*, Clarendon Press: Oxford, 1987.
- ³³ H. C. Andersen, *J. Chem. Phys.* **72**, 2384 (1980).
- ³⁴ D. J. Evans, W. G. Hoover, B. H. Failor, B. Moran, and A. J. C. Ladd, *Phys. Rev. A* **28**, 1016 (1983).
- ³⁵ P. J. Steinhardt, D. R. Nelson, and M. Ronchetti, *Phys. Rev. B* **28**, 784 (1983).
- ³⁶ J. D. Landau and F. M. Lifshitz, *Quantum Mechanics*, Pergamon: New York, 1965.
- ³⁷ R. H. Hardin, N. J. A. Sloane, and W. D. Smith, *Tables of spherical codes with icosahedral symmetry*, published electronically at <http://www.research.att.com/~njas/icosahedral.codes/>.
- ³⁸ Y. Wang and C. Dellago, *J. Phys. Chem. B* **107**, 9214 (2003).
- ³⁹ Note that these values are actually one atom smaller than the magic number N given by Eq. (1). This is because we construct these clusters with a missing central atom, in order to be consistent with the clusters we found from cooling, as described in Section III A.
- ⁴⁰ L. L. Boyer and J. Q. Broughton, *Phys. Rev. B* **42**, 11461 (1990).
- ⁴¹ C. Mottet, G. Treglia, and B. Legrand, *Surf. Sci.* **383**, L719 (1997).
- ⁴² B. M. Ocko, D. Gibbs, K. G. Huang, D. M. Zehner, and S. G. J. Mochrie, *Phys. Rev. B* **44**, 6429 (1991).
- ⁴³ G. Boisvert, L. J. Lewis, M.J. Puska, and R. M. Nieminen, *Phys. Rev. B* **52**, 9078 (1995).
- ⁴⁴ P. J. Feibelman, J. S. Nelson, and G. L. Kellogg, *Phys. Rev. B* **49**, 10548 (1994).
- ⁴⁵ G. Wulff, *Z. f. Kristallog.* **34**, 449 (1901); C. Herring, *Phys. Rev.* **82**, 87 (1931).
- ⁴⁶ C. Jayaprakash, W. F. Saam, and S. Teitel, *Phys. Rev. Lett.* **50**, 2017 (1983).